Characterization of 111 planar defects induced in silicon by hydrogen plasma treatments

Corneliu Ghica, Leona Cristina Nistor, Hugo Bender, Olivier Richard, Gustaaf van Tendeloo, Alexander Ulyashyn

► To cite this version:

Corneliu Ghica, Leona Cristina Nistor, Hugo Bender, Olivier Richard, Gustaaf van Tendeloo, et al.. Characterization of 111 planar defects induced in silicon by hydrogen plasma treatments. Philosophical Magazine, 2006, 86 (32), pp.5137-5151. ⟨10.1080/14786430600801443⟩. ⟨hal-00513718⟩

HAL Id: hal-00513718
https://hal.science/hal-00513718v1

Submitted on 1 Sep 2010

Characterization of {111} planar defects induced in silicon by hydrogen plasma treatments

Journal:	*Philosophical Magazine & Philosophical Magazine Letters*
Manuscript ID:	TPHM-06-Mar-0059.R1
Journal Selection:	Philosophical Magazine
Date Submitted by the Author:	12-May-2006
Complete List of Authors:	Ghica, Corneliu; National Institute for Materials Physics Nistor, Leona; National Institute for Materials Physics Bender, Hugo; IMEC Richard, Olivier; IMEC Van Tendeloo, Gustaaf; University of Antwerp, EMAT Ulyashyn, Alexander; University of Oslo
Keywords:	HRTEM, image processing
Keywords (user supplied):	silicon hydrogenation

Characterization of {111} planar defects induced in silicon by hydrogen plasma treatments

C. GHICA*[†], L. C. NISTOR[†], H. BENDER[‡], O. RICHARD[‡],

G. VAN TENDELOO[§] and A. ULYASHIN[¶]

[†]National Institute for Materials Physics, PO Box MG-7 Magurele, 077125 Bucharest, Romania

[‡]IMEC, Kapeldreef 75, B-3001 Leuven, Belgium

[§]EMAT, University of Antwerp, Groenenborgerlaan 171, B-2020 Antwerpen, Belgium

[¶]University of Oslo, Sem Saelands vei 24, P.O.Box 1048 Blindern, N-0316 Oslo, Norway

A microstructural characterization by transmission electron microscopy of the {111} planar defects induced in Si by treatment in hydrogen plasma is discussed. The {111} defects are analyzed by conventional transmission electron microscopy (TEM) and high-resolution transmission electron microscopy (HRTEM). A quantitative image processing by the geometrical phase method is applied to the experimental high-resolution image of an edge-on oriented {111} defect, in order to measure the local displacements and the strain field around it. Using these data, a structural model of the defect is derived. The validity of the structural model is checked by high-resolution image simulation and comparison with the experimental images.

Keywords: Silicon hydrogenation; HRTEM; Image processing

1. Introduction

Silicon hydrogenation has been intensively studied some decades ago as an important step in the silicon technology. The role played by hydrogen atoms inserted in a silicon matrix, concerning the control of doping atoms activity, defect passivation or suppression of carrier traps, was evidenced and characterized [1-4]. Nowadays, silicon hydrogenation is studied in a new context, namely with the aim of developing and improving a technological method known as ’smart cut‘ used in the fabrication of ’silicon-on-insulator‘ (SOI) substrates [5]. The smart cut technique consists in creating a high density of crystal defects at a certain depth under the surface of a Si wafer and then to remove by an appropriate method the Si layer situated above the mechanically weakened region which contains a high density of defects. The as removed Si layer should remain single crystalline and, ideally, free of defects in order to be used in a multilayer architecture of the kind ’single crystal layer / amorphous insulating layer / single crystal substrate’. The practical way used to induce crystal defects with a certain distribution profile under the Si wafer surface is either by ion implantation or by treatment in a plasma of light atomic species, such as H or He [5-10]. Successful experiments have been reported concerning the smart cut procedure by hydrogen ion implantation, where layers as thin as 200 nm have been removed from the Si wafers [5]. In our research we employ hydrogen plasma in order to induce the necessary amount of defects. Apart from the lower cost, the use of H-plasma instead of H ion implantation could, under the appropriate conditions, be less harmful for the Si layer to be removed by the smart cut. Also, the possibility of peeling off even thinner layers is taken into consideration [11]. In general, the defects induced in Si by H ion implantation or H-plasma treatment are planar defects, bubbles and dislocation loops [12, 13]. The presence of high H concentration levels in the Si lattice somehow complicates the problem, in the sense that the resulting defects are likely decorated with hydrogen and consequently different from the classical crystal defects encountered in Si. In order to be able to control the kind of defects to be induced either by ion implantation or plasma treatment, the identification and characterization of defects in hydrogenated Si is necessary. In a previous paper [14] one has reported about the aspects concerning the surface roughening and the formation of crystal defects in the H-plasma treated Si wafers, as a function of the treatment parameters and the electrical conductivity of the wafer. In this paper we present a qualitative and quantitative characterization of the {111} planar defects in H-plasma treated Si wafers by high-resolution transmission electron microscopy (HRTEM). Based on the strain field data obtained by the quantitative HRTEM image processing, a possible structural model for the defect is derived and verified by HRTEM image simulations.

2. Experimental

In this study we have used *p* and *n*-type (001) Si wafers with different electrical resistivities (1 Ωcm, 4.5 Ωcm and 5 Ωcm) submitted to a 110 MHz RF H-plasma treatment during 1h, 2h and 4h. The wafer temperature during the H-plasma treatment was maintained at 250 ^{o}C. Specimens for transmission electron microscopy (TEM) observations have been prepared in plan-view and cross-section by mechanical polishing and ion milling using a Baltec RES 010 machine. Conventional TEM observations were performed with a Philips CM 20 electron microscope operated at 200 kV, while a JEOL 4000EX electron microscope operating at 400 kV has been used for the HRTEM studies. It is worth mentioning that, during the high-resolution (HR) observations, as a result of the 400 keV electron beam irradiation, crystal defects are created in the Si sample. These are the {113} defects analyzed elsewhere [15, 16] and do not make the subject of this paper. However, being aware of this artifact, we took into consideration only the HR images recorded in the first minute of HR observation in a certain location, before the {113} defects started to form.

3. Results and discussion

In figure 1 the effects of hydrogen plasma irradiation on the morphology and structure of the silicon wafer surface are revealed by conventional TEM. The main features observed are the surface roughening (figures 1b and c) and the presence of three kinds of defects: flower-like defects (type A in figure 1a) observable on plan-view specimens close to ***B*** = [001] zone axis and identified as hydrogen bubbles [12], {111} planar defects (type B) and {001} planar defects (type C), revealed in the cross section specimens. The surface roughening is caused by a preferential etching of the Si wafer in the hydrogen plasma, leading to the formation of micropyramids with {112} crystallographic planes as lateral faces. Throughout this paper, only the {111} planar defects will be analyzed by conventional TEM, HRTEM and HRTEM image processing and simulation.

[Insert figure 1 about here]

3.1 Diffraction contrast analysis

The most frequently encountered defects in hydrogenated Si wafers are disposed along the {111} planes. The slip system in Si is <110>{111}, meaning that dislocations lie along the <110> directions and can slip across the dense {111} planes. The typical example of a planar defect in materials with diamond structure is the stacking fault, resulting from the dissociation of a perfect dislocation into partials. However, the {111} defects in the hydrogenated Si wafers show features which make them different from the classical {111} defects in materials having diamond structure.

Figures 2 and 3 reveal typical conventional TEM images of the {111} defects encountered in the plasma hydrogenated Si samples. The bright field (BF) and dark field (DF) images in figure 2 are obtained in Bragg condition with the $1\bar{1}\bar{1}$ spot strongly excited. Two {111} defects can be observed. One of them, showing fringes, is buried at about 800 nm under the surface. By specimen tilting experiments, we have identified the habit plane for this defect as the (111) plane. The orientation of the reflection vector ***g*** = $(1\bar{1}\bar{1})$ with respect to the bright outer fringe of the planar defect on the dark field image indicates that the defect has an intrinsic character, i.e. has a missing silicon plane [17]. The second defect is seen in edge-on orientation. It is disposed in the $(1\bar{1}\bar{1})$ plane and intercepts the wafer surface.

[Insert figure 2 about here]

As a typical feature for this kind of defects, the characteristic contrast fringes are not straight but slightly curved as can be noticed by comparison with the line drawn on figure 2b. It indicates that the defect is not limited to a single crystallographic plane, but that it affects several adjacent planes.

Information about the displacement vector characterizing the {111} planar defects can be extracted by imaging a defect in Bragg condition using the diffraction spots for which it becomes invisible. Two beam bright field images of such a defect are presented in figure 3, where the $(1\bar{1}1)$ and $(2\bar{2}0)$ reflections have been excited. The characteristic fringes of the defect are visible for ***g*** = $(1\bar{1}1)$, but they become invisible for ***g*** = $(2\bar{2}0)$, showing that the characteristic displacement vector ***R*** has no components along $[2\bar{2}0]$ and is most probably oriented perpendicular to the habit plane, as in the case of regular stacking faults [18].

[Insert figure 3 about here]

3.2 HRTEM observations

In order to accede to the structure of defects at atomic level, HRTEM observations have been performed on {111} defects in edge-on orientation. Figure 4 shows HRTEM images of the {111} planar defects in the plasma hydrogenated silicon, revealed in a very thin part of the specimen (figure 4a) and in a thicker part (figure 4b).

[Insert figure 4 about here]

Figure 4a shows a sharp contrast variation in the defect plane where the columns of atoms are revealed by a much brighter row of dots. In the centre of the figure the defect migrates over two adjacent {111} planes leaving a jog behind. The interpretation of the HRTEM image of the {111} defect in the thicker part of the foil (figure 4b) is less straightforward. This is due to the high strain field accompanying the {111} planar defects in hydrogenated Si specimens. The strain field along the {111} defects is revealed even at low magnifications by diffraction contrast (see the edge-on {111} planar defect in figure 2). This high strain field could be related to the presence of hydrogen decorating these defects. In figure 2, one can see that the strain distribution along the defect is not homogeneous for the defect seen edge on. This might be related to the presence of partial dislocations and jogs which can occur within the thickness of the thin foil. The effect of this high strain field on the HRTEM images strongly alters the contrast along the defect. A variation and even inversion of the phase contrast across the defect can be observed (figure 4b). In regions of higher strain the contrast is almost smeared out. Moreover, the defect is not strictly limited to a single {111} plane, but it migrates to adjacent {111} planes forming jogs. This fact explains the curvature and deformations of the fringes on the diffraction contrast images of the {111} defects. In this situation, proposing a defect structure at atomic level is not an easy task. Moreover, by examining the contrast along the defect plane (figure 4b), a typical contrast consisting of pairs of brighter dots at adjacent rows of dots is frequently observed (arrowed in figure 4b). Several atomic models of the {111} defects in hydrogenated silicon have been proposed, all of them taking into consideration the breaking of the Si-Si bonds along {111} planes and the saturation of the resulting dangling bonds with hydrogen atoms, accompanied by longitudinal and/or transversal shifts of the Si lattice on each side of the defect. Atomic models proposed by Ponce et al. [19], Deák and Snyder [20], Van de Walle et al. [21], Zhang and Jackson [22], Heyman et al. [23] are summarized and simulated as HRTEM images by Muto et al. in Ref. [24].

3.3 HRTEM image processing

In order to decide for a structural model of the {111} defect in plasma hydrogenated Si, we started by processing experimental HRTEM images of {111} defects to determine the strain field around the defect. In the next section we present such an image processing based on the geometrical phase method (GPM) proposed by Hÿtch et al. [25] and using specialized routines under the Digital Micrograph™ 3.3.0 software package for Mac Intosh computers. The geometrical phase method is briefly described in Appendix A.

Figure 5 a reproduces the HRTEM image of the {111} defect in hydrogenated Si in the very thin part of the foil (i.e. figure 4a), while figure 5b gives its Fourier transform. An XY coordinate system has been chosen and indicated near the left low corner of the HR picture.

[Insert figure 5 about here]

As in a diffraction pattern of a thin foil containing planar defects, the spots in the FFT spectrum show streaks oriented perpendicular to the planar defect in the HRTEM image. The phase images in figures

5c and d have been obtained by selecting with a Gaussian mask the $\bar{1}11$ and $\bar{2}2\bar{4}$ spots in figure 5b, respectively. The local phase across the images is calculated with respect to the average phase value corresponding to a reference area delimited by a rectangle in the low part of the phase images. The size and position of this reference area are chosen in such a way to eliminate regions showing stray $+\pi$ / $-\pi$ phase jumps not related to the defect. On the phase images white / black areas correspond to regions of higher (positive) / lower (negative) phase, while grey areas are in phase (zero) with the reference area. One can notice on figure 5c, on the $\boldsymbol{g_1}$ phase image (Φ_{g1}), a clear phase jump of the $\bar{1}11$ fringes across the defect with respect to the reference area.

Using the two phase images, the displacement field $\boldsymbol{u}(\boldsymbol{r})$ can be calculated according to equation (A4) in Appendix A. The two real space vectors corresponding to the reciprocal $\boldsymbol{g_1} = [\bar{1}11]*$ and $\boldsymbol{g_2} = [\bar{2}2\bar{4}]*$ vectors are $\boldsymbol{a_1} = 1/3[\bar{1}11]$ and $\boldsymbol{a_2} = 1/12[\bar{1}1\bar{2}]$. In the picture coordinate system XY, $\boldsymbol{a_1}$ is parallel to the OY axis and $\boldsymbol{a_2}$ parallel to the OX axis. The displacement field $\boldsymbol{u}(\boldsymbol{r})$ can be mapped by imaging its $u_x(\boldsymbol{r})$ and $u_y(\boldsymbol{r})$ components according to the equations:

$$u_x(\boldsymbol{r}) = (-1/2\pi)[\Phi_{g1}(\boldsymbol{r})a_{1x} + \Phi_{g2}(\boldsymbol{r})a_{2x}]$$

$$u_y(\boldsymbol{r}) = (-1/2\pi)[\Phi_{g1}(\boldsymbol{r})a_{1y} + \Phi_{g2}(\boldsymbol{r})a_{2y}] \qquad (1)$$

In our picture coordinate system $a_{1x} = 0$, $a_{1y} = |\boldsymbol{a_1}| = \sqrt{3}/3$ and $a_{2x} = |\boldsymbol{a_2}| = \sqrt{6}/12$, $a_{2y} = 0$, which turns equation (1) into:

$$u_x(\boldsymbol{r}) = -(\sqrt{6}/24\pi)\Phi_{g2}(\boldsymbol{r})$$

$$u_y(\boldsymbol{r}) = -(\sqrt{3}/6\pi)\Phi_{g1}(\boldsymbol{r}) \qquad (2)$$

expressed in fractions of the lattice parameter, a, or:

$$u_x(\boldsymbol{r}) = -0.176\Phi_{g2}(\boldsymbol{r})$$

$$u_y(\boldsymbol{r}) = -0.499\Phi_{g1}(\boldsymbol{r}) \qquad (3)$$

expressed in nm (the lattice parameter of Si is a_{Si}=0.543 nm).

The u_x and u_y components of the strain field calculated with (3) are depicted in figures 5e and f where, again grey means no displacement, white means positive displacement (in the positive sense of the coordinate axis) and dark means negative displacement. In figure 5f one can notice an uniform negative rigid body displacement along OY (or $[\bar{1}11]$ direction) of the upper part of the image with respect to the reference area. The phase jump as well as the displacement field can be quantitatively expressed using line profiles across the defect. In order to reduce the influence of the noise, the line profile has been averaged over the 8 nm width of the rectangle figured in the left hand side of the Φ_{g1} and u_y images, figures 5c and f. Thus, the phase jump revealed by the line profile across the defect in the positive sense of the OY axis (figure 5g) measures $0.72\pi \pm 0.044$ radians. Correspondingly, the value of the u_y displacement measured on the line profile (figure 5h) is 0.116 ± 0.002 nm. It is worth to notice that the phase jump is not steep, but it occurs over approximately 2 nm across the defect. Accordingly, the displacement field u_y shows a finite gradient across the defect. Thus, a jump of 0.116 nm takes place over a range of about 2 nm around the planar defect.

The displacement gradient corresponds to a strain that can be calculated according to equations (A5) and (A6) in Appendix A. The three components of the symmetrical strain matrix ε_{ij} are graphically represented in figures 5 i-k, where bright and dark means tensile and compressive strain, respectively. One can notice that the defect is characterized by a well defined ε_{yy} compressive strain confined to a narrow region around the defect (figure 5j). The line profile of ε_{yy} across the defect, averaged over the width of the rectangle (8 nm) marked in the left part of the image in figure 5j, is asymmetrical and shows two minima, one of 13% and the other of 8%. The width of the 2-peaked structure, defined as the range between the positions corresponding to 10% of the minimum value, measures about 2.2 nm. By comparing the ε_{yy} strain image (figure 5j) with the original experimental HRTEM image (figure 5a), one can see that the two minima of the strain field actually refer to the position of the two rows of bright dots adjacent to the brighter row of dots revealing the defect.

The existence of a strain field around the {111} planar defect in hydrogenated Si represents a major difference from the {111} stacking faults encountered in *fcc* materials, which show no strain far from the limiting partial dislocations. The presence of a strain, significant through both its amplitude and range around the {111} planar defect in hydrogenated Si wafers, should be related to the presence of hydrogen decorating the planar defects. Previous Raman measurements [14] revealed the existence of hydrogen in these specimens. In our opinion, inside the Si lattice, hydrogen acts in two ways: on one hand, due to its high chemical reactivity, it forms volatile Si-H compounds leading to the removal of Si atoms from the lattice; on the other hand, it saturates the resulting Si dangling bonds, as we will further show in the proposed models for the {111} defect.

3.3 HRTEM image simulation

In order to derive a structural model of the defect, we used the results provided by the quantitative image processing in the previous section. As we have shown by conventional TEM and confirmed by the GPM analysis, the displacement vector characterizing the {111} defect is oriented perpendicular to the defect plane and has no component parallel to it (u_x=0). The average value of the displacement, obtained by the GPM analysis is $|\boldsymbol{R}| = u_y = -0.116 \pm 0.002$ nm, i.e. $-1/2.7\ d_{111}$ hence larger than the displacement field for a stacking fault.

We used the Crystal Kit software for the structural modelling of the defect. Starting from the undistorted Si crystal structure projected along [110] (figure 6a), the 0.116 nm rigid body displacement has been applied to the upper part of the matrix with respect to the fixed bottom part. Two structural models (*A* and *B*) can be derived using the same displacement value. In one case, only one layer of Si atoms adjacent to the interface has been removed (model *A* in figure 6b), while in the second case both Si layers close to the interface have been removed (model *B* in figure 6c). In both cases, we consider that the resulting dangling bonds are saturated with hydrogen.

[Insert figure 6 about here]

A unit cell has been defined in each case and simulated HR images have been calculated using the Mac Tempas software. In figures 7a and b we present a series of simulated images obtained for different values for the lens defocus and specimen thickness, corresponding to the two structural models. At a visual inspection of the simulated images based on the two structural models and a qualitative comparison with the experimental images, we can conclude that model *B* provides a better fit for the HR images of the defect. Thus, the defect is imaged either as a single row of brighter dots in the thin areas of the specimen, as in figure 4a, or as a double row of bright dots in the thicker regions, as in figure 4b.

[Insert figure 7 about here]

The structural model in figure 6c corresponds to the H_2* defect model described in literature [26], where the Si-Si chemical bonds were cut and the hydrogen atoms saturate the resulting dangling bonds. Indeed, in the case of model *B*, where two rows of Si atoms are removed, the defect can be chemically stabilized by saturating with H the dangling bonds of the two rows of Si atoms adjacent to the defect plane. Consequently, the planar defect could be described as a collection of H_2* defects lined up on a {111} plane.

Model *B* seems to be favoured from the chemical and energetic point of view against model *A*. An enlarged structural model of the atoms arrangement close to the defect plane for the two models *A* and *B* is shown in figure 6d and e, respectively, where the real distances (not the projected ones) between the Si atoms are specified in nm. The chemical bonds are also figured for the atoms limiting the defect. We mention that these models do not take into consideration any atomic relaxation around the defect. In the case of model *A*, one sees that the shortest distance between the Si atoms bordering the defect is 0.297 nm instead of 0.235 nm as in a perfect structure. Consequently, there are two possibilities of saturating the dangling bonds:

i. The Si atoms delimiting the defect remain unbound and the dangling bonds, one for each Si atom limiting the defect from the upper crystal and three for each Si atom limiting the defect from the bottom crystal, are saturated with H atoms (marked with (1) on figure 6d);

ii. The formation of a stretched bond between the Si atoms delimiting the defect and saturation with H atoms of the two remaining dangling bonds belonging to the Si atoms limiting the defect from the bottom crystal (marked with (2) on figure 6d).

The two variants of the model *A* need either an increased number of H atoms for the saturation of the dangling bonds, or the formation of a stretched chemical bond, which is energy costly. Model *B* (enlargement in figure 6e) seems much more plausible, since it only involves Si-Si bonds cutting and saturation of the resulting dangling bonds with H atoms, one for each Si atom neighbouring the defect. The defect could be physically formed by removing the Si atoms from the structure as a result of the etching effect of the H-plasma on the Si wafer.

4. Conclusions

Si wafer exposure to a hydrogen RF-plasma leads to the formation of specific crystal defects decorated with H atoms. In this paper we have analyzed the typical {111} defects induced in Si by plasma hydrogenation. We have described the diffraction contrast characteristics and studied the high-resolution images of edge-on oriented {111} defects. The information extracted from the diffraction contrast images about the intrinsic character of the defect and the habit plane has been confirmed by the HR observations. HRTEM images show that the defect is not limited to a single {111} plane, but it shows jogs and migrates to adjacent {111} planes. Quantitative image processing by the geometrical phase method of the HRTEM image of an edge-on {111} defect has revealed the intrinsic character of the defect and provided quantitative information about the lattice strain around the {111} defects. The existence of a lattice strain around the defects due to decorating H atoms makes them different from the simple stacking faults. The quantitative information derived by image processing has been used as input for the structural modelling of the defect, resulting in two possible models. Simulated HR images based on the two structural models have been compared with the experimental images of the defect. We have shown that only one of the two possible structural models provides simulated HR patterns that fit well the experimental images, both for the small and larger thicknesses of the specimen. This structural model corresponds to the H_2* defect described in literature, which seems more favoured from the chemical and energetic points of view.

Acknowledgements

This work is part of the bilateral Flemish-Romanian research project BIL 01/73, with support from the Romanian Ministry of Education and Research (project CERES 4-43/2004).

Appendix A: Short description of the Geometrical Phase Method

The Geometrical Phase Method (GPM) [25] considers the HRTEM image of the perfect crystal as a 2D periodic pattern, which can be described as a Fourier series:

$$I(\boldsymbol{r}) = \sum_{g} I_g(\boldsymbol{r}) \exp(2\pi i \boldsymbol{g} \cdot \boldsymbol{r}) \qquad \text{(A1)}$$

where $I_{\boldsymbol{g}}(\boldsymbol{r})$ is the Fourier component corresponding to the reciprocal vector $\boldsymbol{g}$. In the HRTEM image of a thin foil containing structural defects, the complex, locally varying Fourier components are characterized by an amplitude $A_{\boldsymbol{g}}(\boldsymbol{r})$ and a phase $\Phi_{\boldsymbol{g}}(\boldsymbol{r})$, both depending on the position in the image.

$$I_g(\boldsymbol{r}) = A_g(\boldsymbol{r}) \exp(i\Phi_g(\boldsymbol{r})) \qquad \text{(A2)}$$

The amplitude $A_{\boldsymbol{g}}(\boldsymbol{r})$ gives the local contrast of the HRTEM fringes corresponding to $\boldsymbol{g}$, while the phase $\Phi_{\boldsymbol{g}}(\boldsymbol{r})$ represents the local shift of the HRTEM fringes from their ideal position (*geometrical* phase), due to the presence of a lattice defect. The geometrical phase $\Phi_{\boldsymbol{g}}(\boldsymbol{r})$ may be described either in terms of local displacement $\boldsymbol{u}(\boldsymbol{r})$ of the fringes from their undistorted position, or as a local variation of the fringe interspacing (i.e. variation of $\boldsymbol{g}$):

$$\Phi_g(\boldsymbol{r}) = -2\pi \boldsymbol{g} \cdot \boldsymbol{u}(\boldsymbol{r}) \quad \text{or} \quad \Phi_g(\boldsymbol{r}) = 2\pi \Delta \boldsymbol{g} \cdot \boldsymbol{r} \qquad \text{(A3)}$$

By selecting with an appropriate mask an individual spot $\boldsymbol{g_1}$ from the fast Fourier transform (FFT) image, one can extract by inverse Fourier transformation the *phase image* $\Phi_{\boldsymbol{g_1}}(\boldsymbol{r})$, representing the local shift of the corresponding family of fringes from their ideal position in an undistorted crystal.

The local phase is calculated with respect to an undistorted reference area on the image, far from the strain field of the defect. A second phase image $\Phi_{\boldsymbol{g2}}(\boldsymbol{r})$ can be obtained by moving the selecting mask on a different vector $\boldsymbol{g_2}$, noncollinear with $\boldsymbol{g_1}$. Using the two phase images, one can calculate and display the image showing the vectorial displacement field:

$$\boldsymbol{u}(\boldsymbol{r}) = (-1/2\pi)[\Phi_{g1}(\boldsymbol{r})\boldsymbol{a_1} + \Phi_{g2}(\boldsymbol{r})\boldsymbol{a_2}] \qquad \text{(A4)}$$

where $\boldsymbol{a_1}$ and $\boldsymbol{a_2}$ represent the real space vector basis corresponding to the reciprocal lattice vectors $\boldsymbol{g_1}$

and $\boldsymbol{g}_2$. By further derivation of the local fringe displacement $\boldsymbol{u}(\boldsymbol{r})$, one can calculate and map the matrix **e** of the local lattice distortion:

$$\mathbf{e} = \begin{pmatrix} e_{xx} & e_{xy} \\ e_{yx} & e_{yy} \end{pmatrix} = \begin{pmatrix} \partial u_x / \partial x & \partial u_x / \partial y \\ \partial u_y / \partial x & \partial u_y / \partial y \end{pmatrix} \qquad \text{(A5)}$$

where $\boldsymbol{r}=(x, y)$ represents the local coordinates in the image. The strain field and the rigid rotation of the lattice around the defect are expressed, respectively, by a symmetrical matrix $\boldsymbol{\varepsilon}$ and an asymmetrical one $\boldsymbol{\omega}$, given by:

$$\boldsymbol{\varepsilon} = 1/2\,(\mathbf{e} + \mathbf{e}^T)$$

$$\boldsymbol{\omega} = 1/2\,(\mathbf{e} - \mathbf{e}^T) \qquad \text{(A6)}$$

where T denotes the transpose of the matrix.

References

[1] J.I. Pankove, D.E. Carlson, J.E. Berkeyheiser, R.O. Wance, Phys. Rev. Lett. **51** 2224 (1983).

[2] N.M. Johnson, Phys. Rev. B **31** 5525 (1985).

[3] N.M. Johnson, S.K. Hahn, Appl. Phys. Lett. **48** 709 (1986).

[4] W.E. Spear, P.G. LeComber, Solid State Comm. **17** 1193 (1975).

[5] M. Bruel, Nucl. Instr. and Meth. in Phys. Reas. B **108** 313 (1996).

[6] N.M. Johnson, F.A. Ponce, R.A. Street, R.J. Nemanich, Phys. Rev. B **35** 4166 (1987).

[7] S.J. Jeng, G.S. Oehrlein, G.J. Scilla, Appl. Phys. Lett. **53** 1735 (1988).

[8] S. Rangan, S. Ashok, G. Chen, D. Theodore, Nucl. Instr. and Meth. in Phys. Reas. B **206** 417 (2003).

[9] C. Qian, B. Terreault, S.C. Gujrathi, Nucl. Instr. and Meth. in Phys. Reas. B **175-177** 711 (2001).

[10] P.F.P. Fichtner, J.R. Kaschny, M. Behar, R.A. Yankov, A. Mücklich, W. Skorupa, Nucl. Instr. and Meth. in Phys. Reas. B **148** 329 (1999).

[11] A. Y. Ushenko, A. G. Ulyashin, Jpn. J. Appl. Phys. **41** 5021 (2002).

[12] C. Ghica, L. Nistor, O. Richard, H. Bender, A. Ulyashin, G. Van Tendeloo, *Proceedings to 13th European Microscopy Congress EMC 2004*, II 395 (2004).

[13] C. Ghica, L. Nistor, O. Richard, H. Bender, A. Ulyashin, G. Van Tendeloo, *Proceedings to 13th European Microscopy Congress EMC 2004*, II 405 (2004).

[14] A.G. Ulyashin, R. Job, W.R. Fahrner, O. Richard, H. Bender, C. Claeys, E. Simoen, D. Grambole, J. of Phys.: Condens. Matter **14** 13037 (2002).

[15] L. Fedina, A. Gutakovskii, A. Aseev, J. Van Landuyt, J. Vanhellemont, Phys. Stat. Sol. (a) **171** 147 (1999).

[16] L. Fedina, A. Gutakovskii, A. Aseev, J. Cryst. Growth **229** 1 (2001).

[17] G. Saada, *Microscopie électronique des lames minces cristallines* (Masson & C^{ie}, Paris, 1966), pp.

235-237.

[18] P.B. Hirsch, A. Howie, R.B. Nicholson, D.W. Pashley, M.J. Whelan, *Electron Microscopy of Thin Crystals* (Butterworth & Co., London, 1967), pp. 165.

[19] F.A. Ponce, N.M. Johnson, J.C. Tramontana, J. Walker, Inst. Phys. Conf. Ser. **87** 49 (1987).

[20] P. Deák, L. C. Snyder, Radiat. Effects **111-112** 77 (1989).

[21] C.G. Van De Walle, P.J.H. Denteneer, Y. Bar-Yam, S. Pantelides, Phys. Rev. Lett. **60** 2761 (1989).

[22] S.B. Zhang, W.B. Jackson, Phys Rev. B **43** 12142 (1991).

[23] J.N. Heyman, J.W. Ager III, E.E. Haller, N.M. Johnson, J. Walker, C.M. Doland, Phys. Rev. B **45** 13363 (1992).

[24] S. Muto, S. Takeda, M. Hirata, Phil. Mag. A **72** 1057 (1995).

[25] M.J. Hÿtch, E. Snoeck, R. Kilaas, Ultramicroscopy **74** 131 (1998).

[26] M.K. Weldon, V.E. Marsico, Y.J. Chabal, A. Agarwal, D.J. Eaglesham, J. Sapjeta, W.L. Brown, D.C. Jacobson, Y. Caudano, S.B. Christman, E.E. Chaman, J. Vac. Sci. Technol. B **15** 1065 (1997).

Figure captions

Figure 1. Typical TEM images of the Si:H wafers showing three kinds of defects induced by treatment in RF H-plasma: (a) plan-view image close to ***B***=[001] showing flower-like defects (bubbles) with 4-fold symmetrical strain field contours; (b) cross-section image close to ***B***=[110] showing the surface roughening and planar defects along the {111} planes (B-type); (c) cross-section image close to ***B***=[110] showing the surface roughening and two kinds of planar defects, along the {111} planes (B-type) and {100} planes (C-type).

Figure 2. Bright field (a) and dark field (b) images of a planar {111} defect. 'T' and 'B' denote, respectively, the top and bottom ends of the planar defect intercepting the specimen surfaces. The black line on the DF image has been added as a reference in order to evidence the fringe curvature.

Figure 3. Bright field TEM images in Bragg condition of a {111} planar defect using the $1\bar{1}1$ (a, b) and $2\bar{2}0$ (c, d) reflections.

Figure 4. Typical HRTEM images of the {111} defect in hydrogenated Si in thin (a) and thick (b) regions of the specimen. In (b) the arrows indicate regions along the planar defect showing the typical high-resolution contrast.

Figure 5. (a) HRTEM image of the {111} defect in the thin region; the assigned XY coordinate system is figured; (b) Fourier transform of the HRTEM image; (c), (d) Phase images Φ_{g1} and Φ_{g2} obtained by FFT^{-1} using a Gaussian mask around $\boldsymbol{g_1}=\bar{1}11$ and $\boldsymbol{g_2}=\bar{2}2\bar{4}$, respectively; (e), (f) $u_x(\boldsymbol{r})$ and $u_y(\boldsymbol{r})$ components of the displacement field $\boldsymbol{u}(\boldsymbol{r})$ around the defect; (g) line profile of the phase across the

defect in the Φ_{g1} phase image averaged over the 8 nm width of the rectangle in the left part of the image; (h) line profile of the $u_y(\boldsymbol{r})$ component across the defect in the positive sense of the OY axis; (i), (j), (k) maps of the ε_{xx}, ε_{yy} and ε_{xy} components of the symmetrical strain matrix $\boldsymbol{\varepsilon}_{\mathbf{ij}}$; (l) line profile of the strain component ε_{yy} across the defect.

Figure 6. Possible structural models of the {111} defect based on the displacement values obtained by the GPM analysis. (a) Undistorted Si structure projected along [110]; the horizontal line marks the interface between the bottom fixed part of the crystal and the upper part to which the displacement vector is applied; (b) structural model *A* of the {111} defect where one Si layer has been removed; (c) structural model *B* of the {111} defect where two Si layers have been removed; (d) and (e) enlarged view of the atomic arrangement close to the defect plane for models *A* and *B*, respectively; interatomic distances in nm are indicated.

Figure 7. Matrices of simulated HR images for various thickness and defocus values based on the structural models *A* (a) and *B* (b).

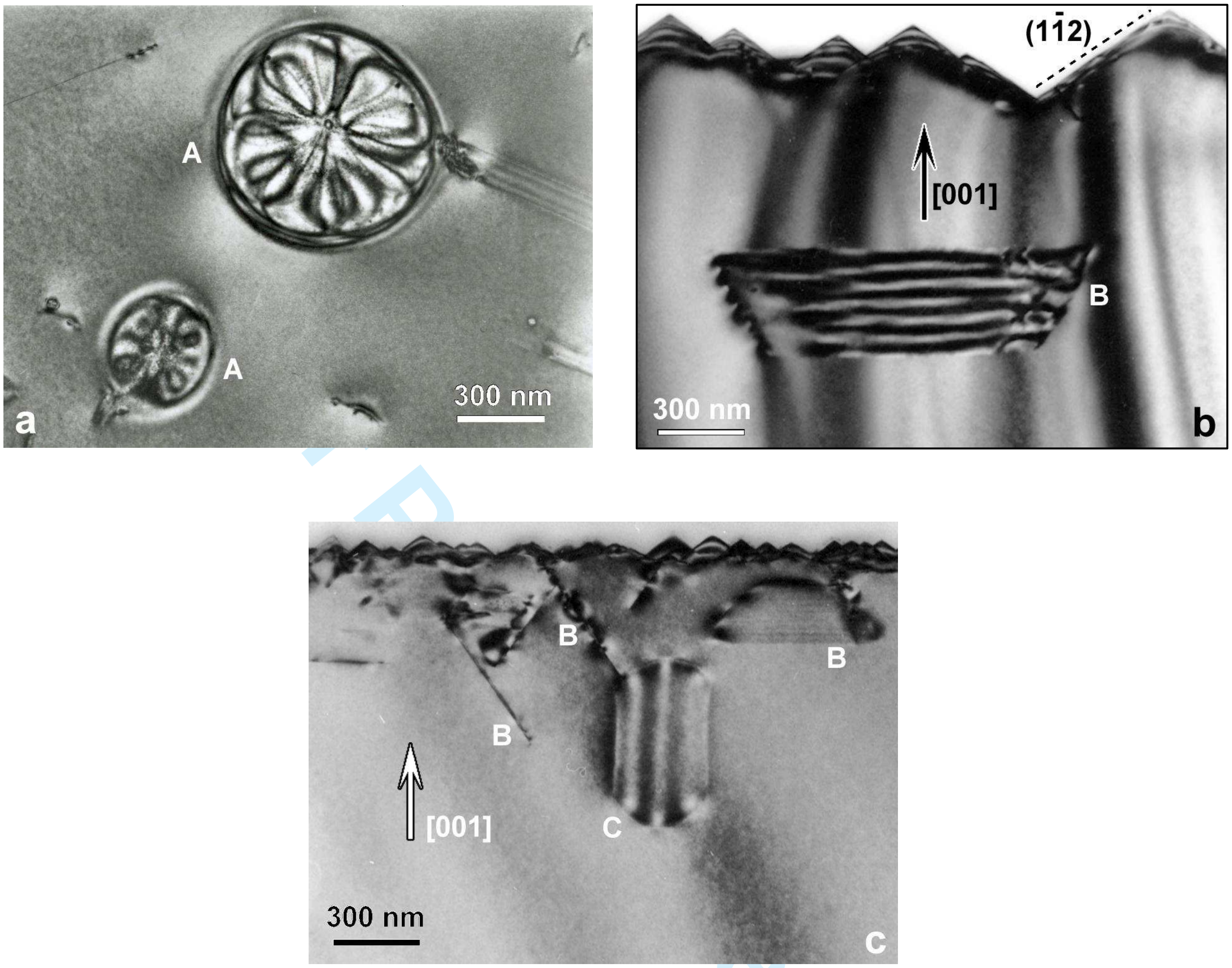

Figure 1.

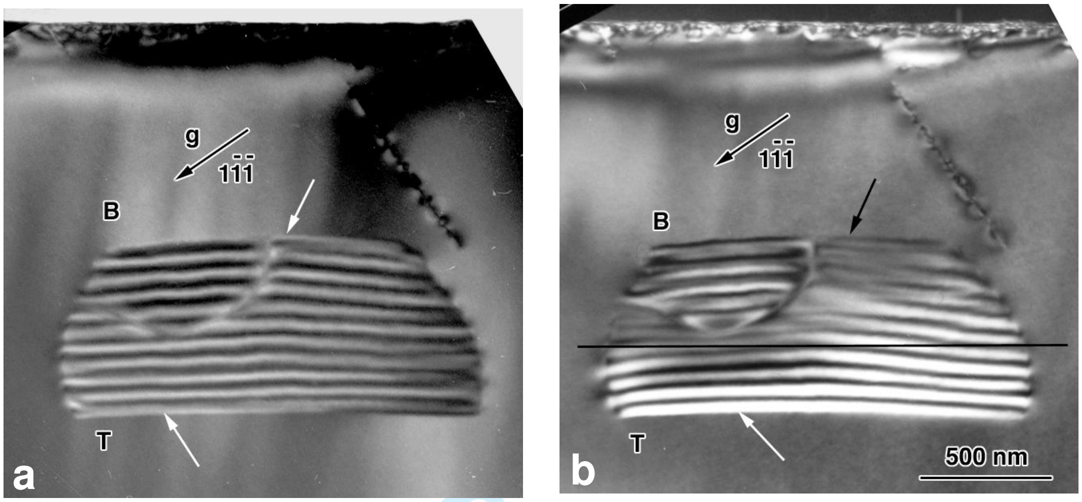

Figure 2.

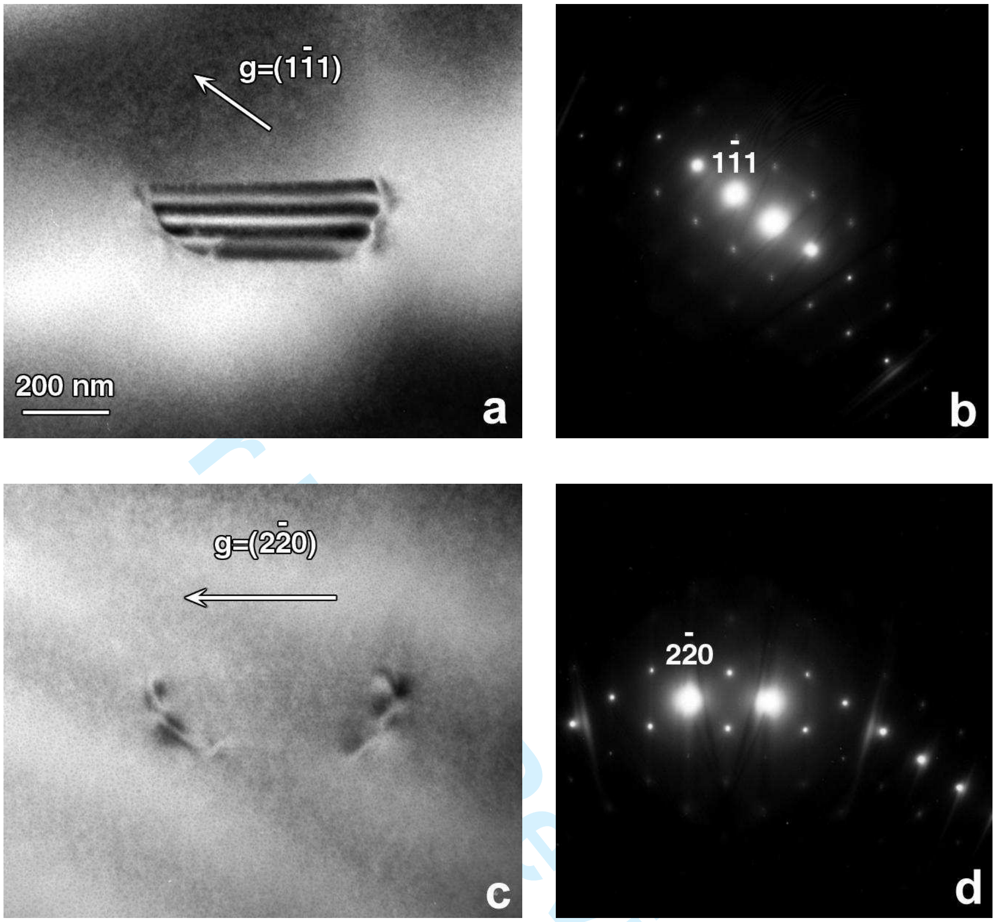

Figure 3.

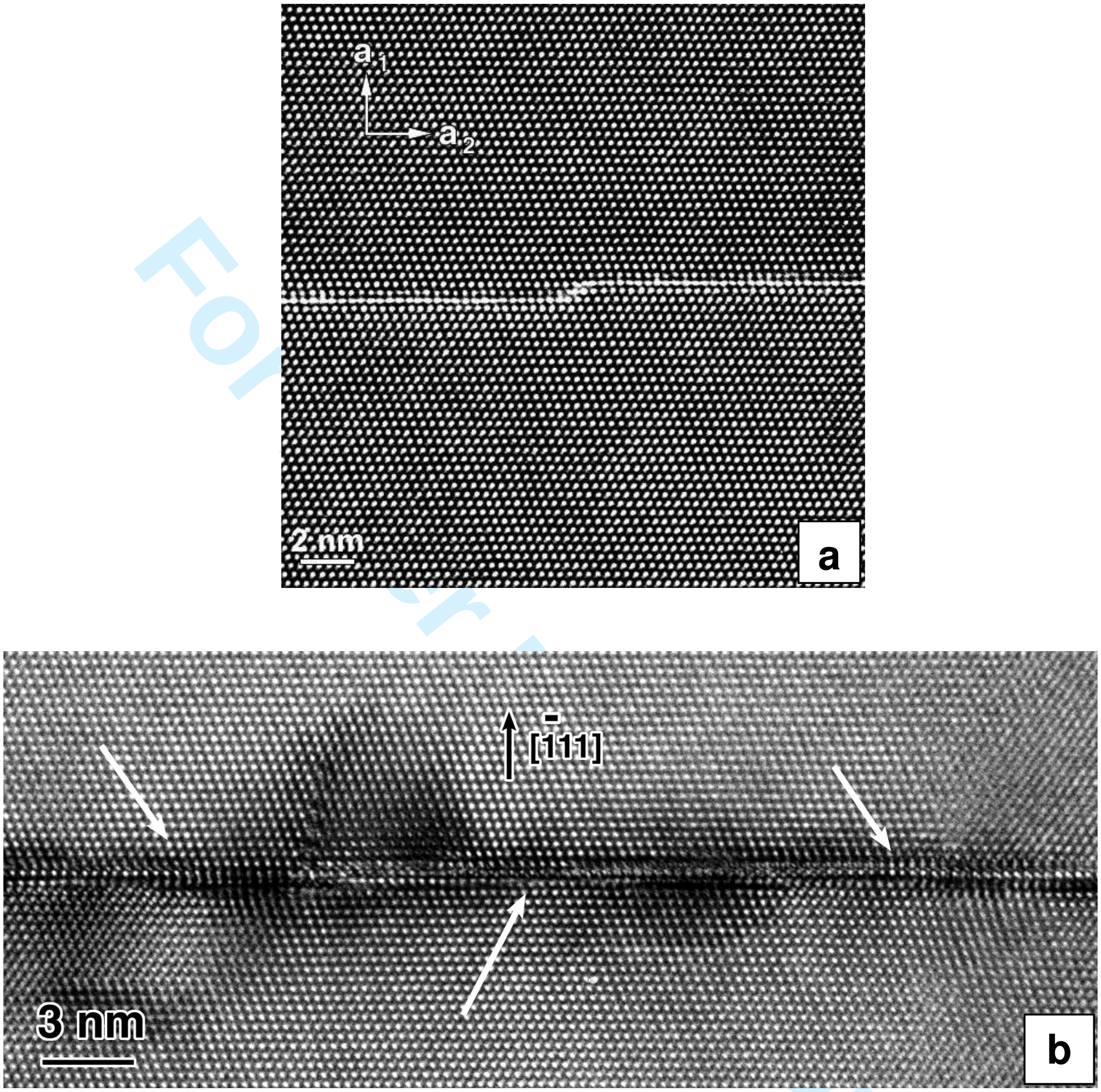

Figure 4.

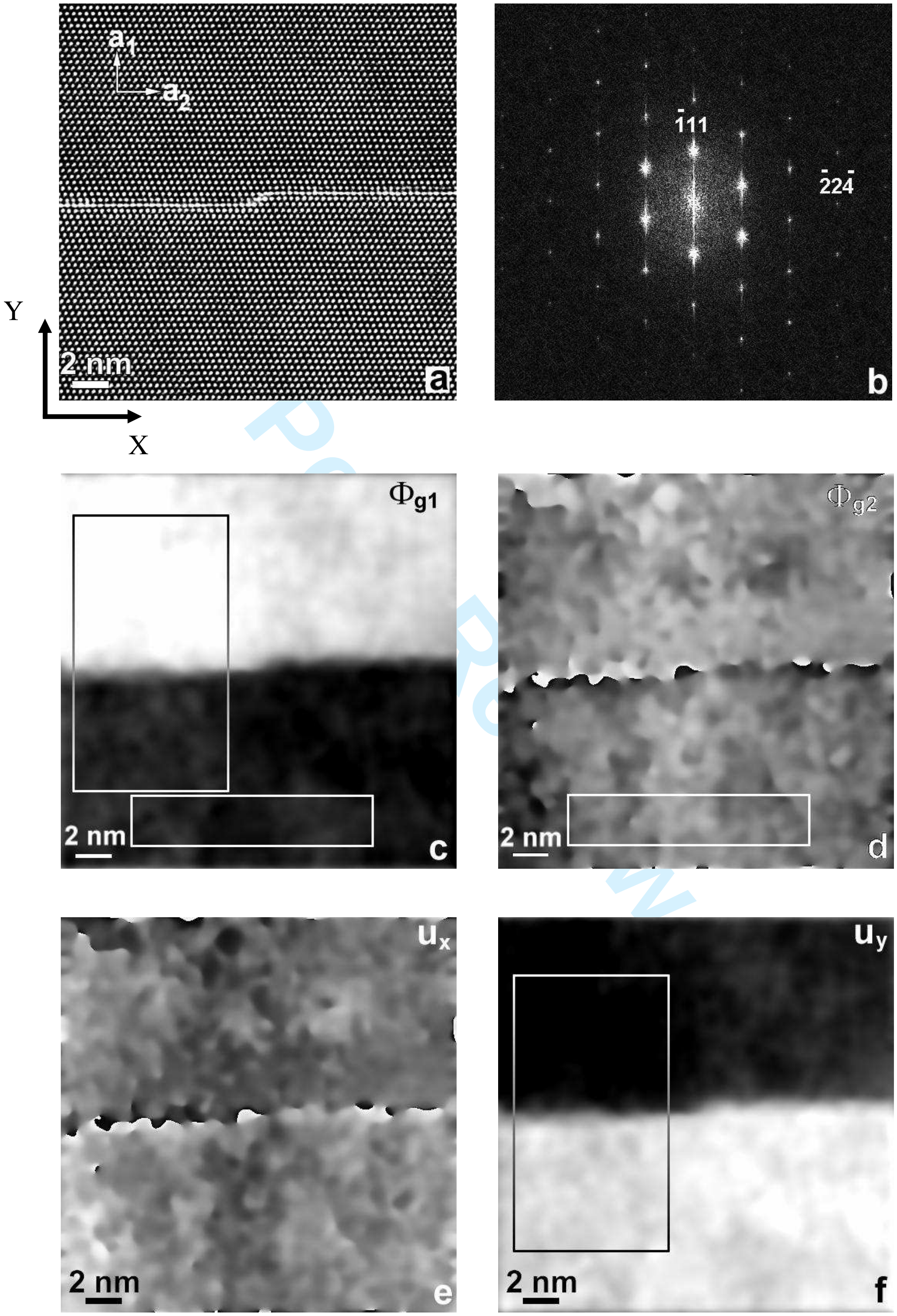
a_1
a_2
Y
X
2 nm
a
$\bar{1}11$
$\bar{2}2\bar{4}$
b
Φ_{g1}
2 nm
c
Φ_{g2}
2 nm
d
u_x
2 nm
e
u_y
2 nm
f

Figure 5.

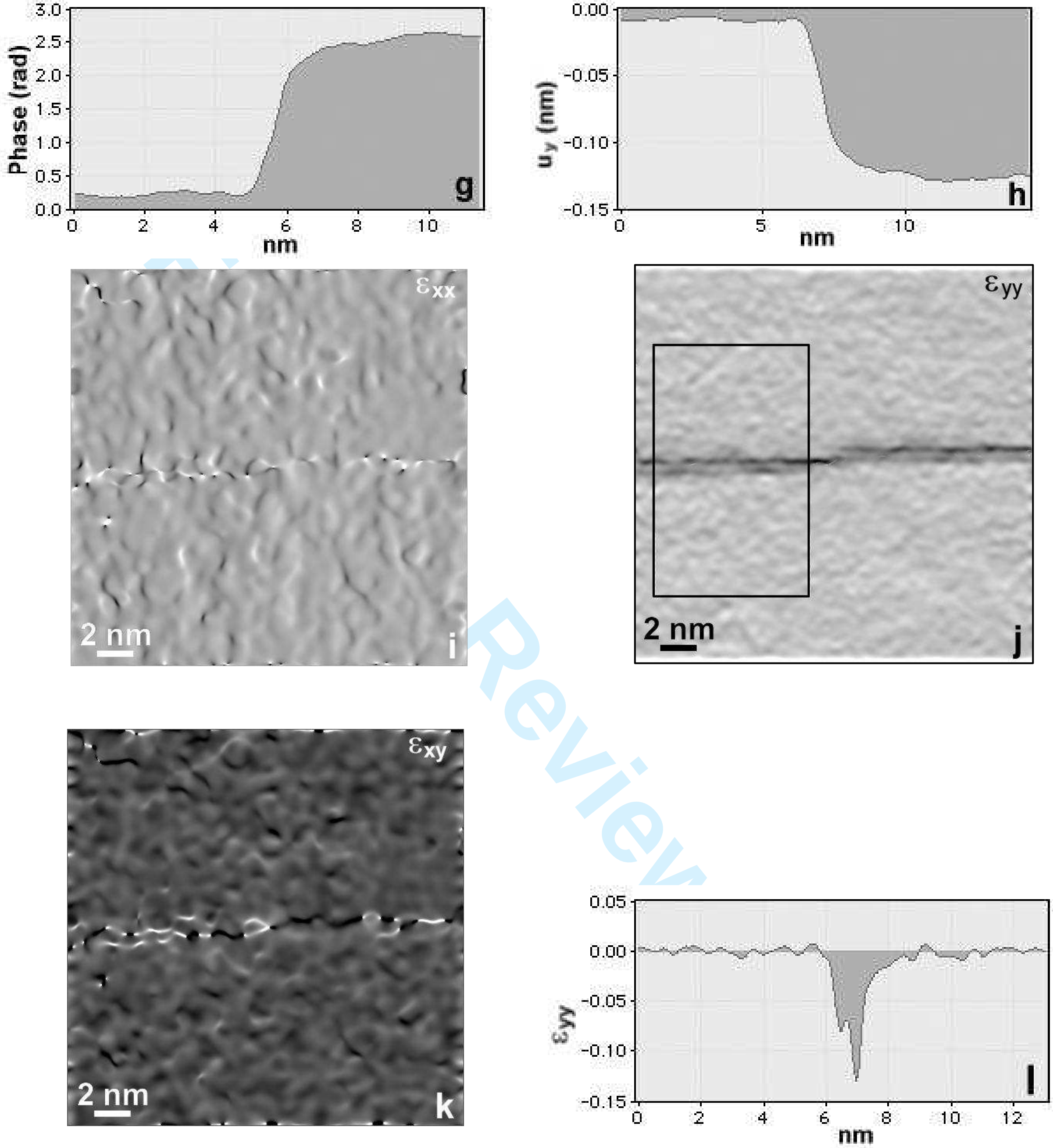

Figure 5 continued.

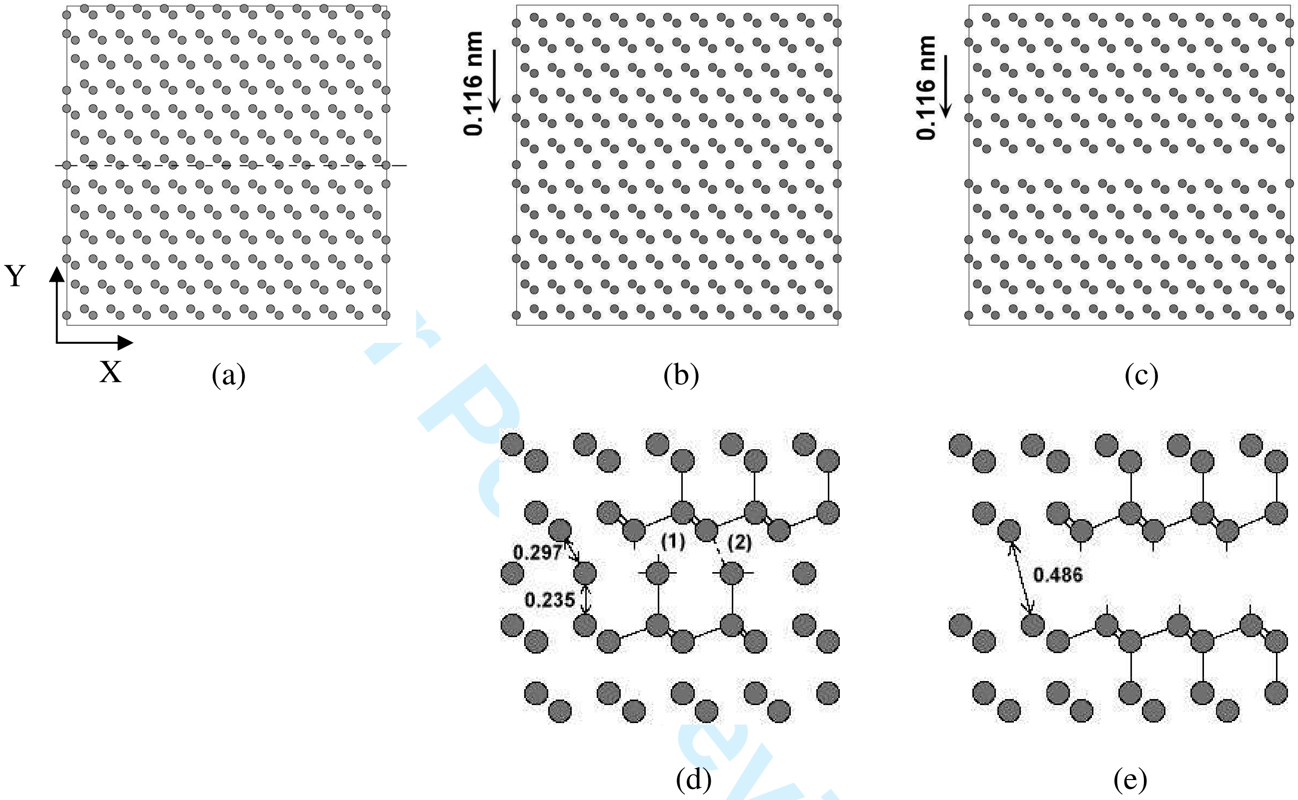

(a) (b) (c)

(d) (e)

Figure 6.

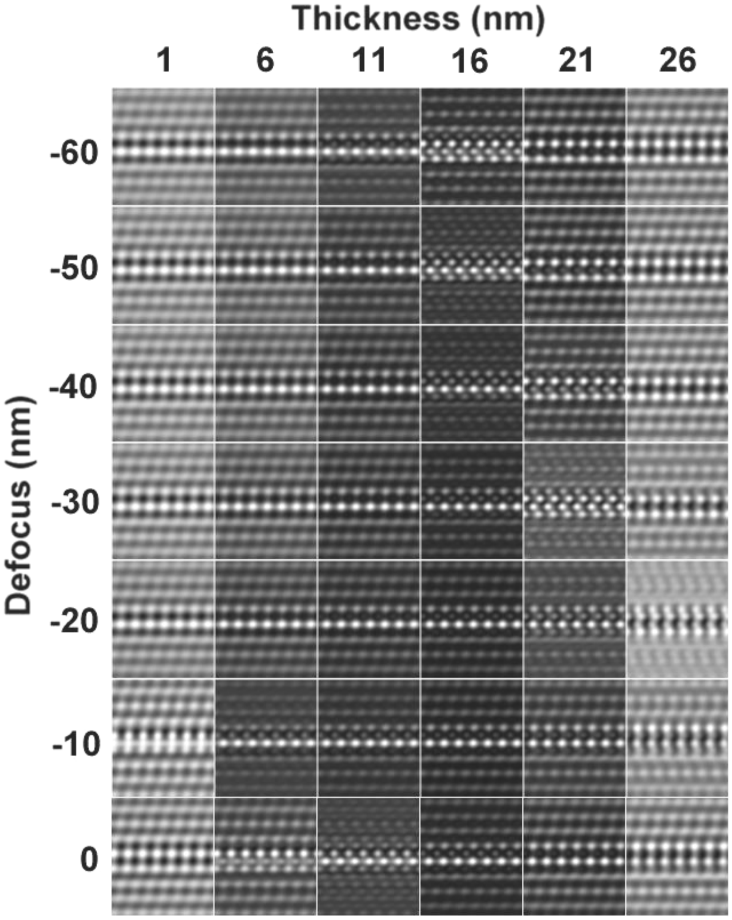

(a)

Figure 7.

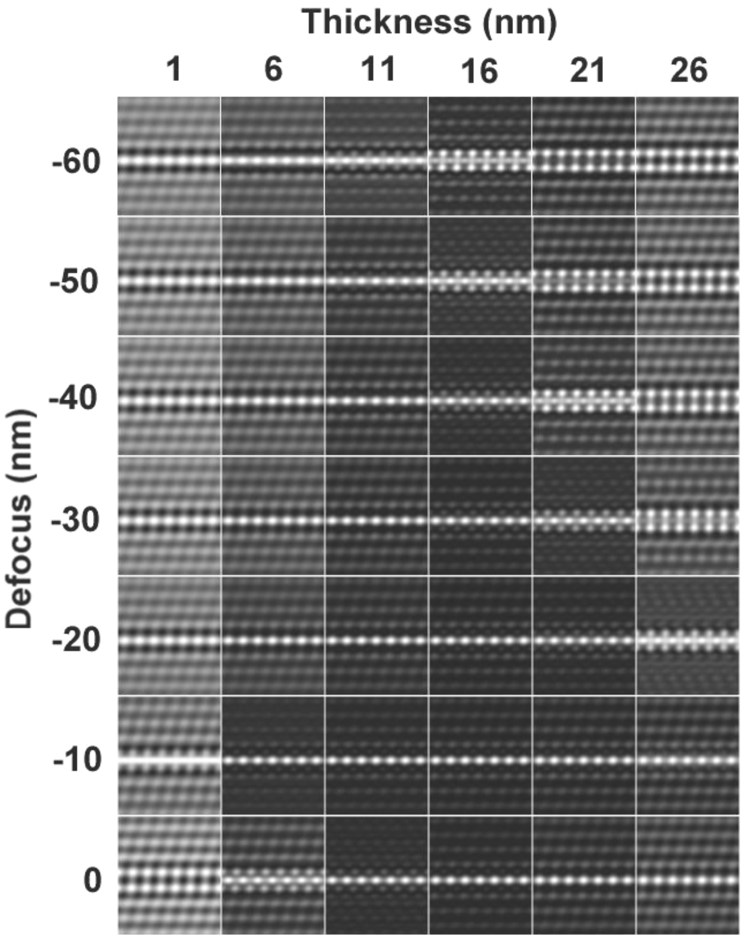

(b)

Figure 7 continued.